Acta Oceanol. Sin., 2020, Vol. 39, No. 8, P. 1–13
https://doi.org/10.1007/s13131-020-1617-x
http://www.hyxb.org.cn
E-mail: hyxbe@263.net

Impact of warm mesoscale eddy on tropical cyclone intensity

Jia Sun[1, 2], Guihua Wang[3]*, Xuejun Xiong[1, 2], Zhenli Hui[1, 2], Xiaomin Hu[1, 2], Zheng Ling[4], Long Yu[1, 2], Guangbing Yang[1, 2], Yanliang Guo[1, 2], Xia Ju[1, 2], Liang Chen[1, 2, 5]

[1] First Institute of Oceanography, Ministry of Natural Resources, Qingdao 266061, China

[2] Laboratory for Regional Oceanography and Numerical Modeling, Pilot National Laboratory for Marine Science and Technology (Qingdao), Qingdao 266237, China

[3] Institute of Atmospheric Sciences, Department of Environmental Science and Engineering, Fudan University, Shanghai 200433, China

[4] Guangdong Key Laboratory of Coastal Ocean Variability and Disaster Prediction, Guangdong Ocean University, Zhanjiang 524088, China

[5] College of Oceanic and Atmospheric Sciences, Ocean University of China, Qingdao 266100, China

Received 25 December 2019; accepted 5 March 2020

Abstract

The spatial-temporal patterns of tropical cyclone (TC) intensity changes caused by the warm ocean mesoscale eddy (WOME) distribution are evaluated using two sets of idealized numerical experiments. The results show that the TC was intensified and weakened when a WOME was close to and far away from the TC center, respectively. The area where the WOME enhanced (weakened) TC intensity is called the inner (outer) area in this study. Amplitudes of the enhancement and weakening caused by the WOME in the inner and outer area decreased and increased over time, while the ranges of the inner and outer area diminished and expanded, respectively. The WOME in the inner area strengthened the secondary circulation of the TC, increased heat fluxes, strengthened the symmetry, and weakened the outer spiral rainband, which enhanced TC intensity. The effect was opposite if the WOME was in the outer area, and it weakened the TC intensity. The idealized simulation employed a stationary TC, and thus the results may only be applied to TCs with slow propagation. These findings can improve our understanding of the interactions between TC and the WOME and are helpful for improving TC intensity forecasting by considering the effect of the WOME in the outer areas.

Key words: tropical cyclone intensity, warm ocean mesoscale eddy, upper ocean, spatial-temporal pattern

Citation: Sun Jia, Wang Guihua, Xiong Xuejun, Hui Zhenli, Hu Xiaomin, Ling Zheng, Yu Long, Yang Guangbing, Guo Yanliang, Ju Xia, Chen Liang. 2020. Impact of warm mesoscale eddy on tropical cyclone intensity. Acta Oceanologica Sinica, 39(8): 1–13, doi: 10.1007/s13131-020-1617-x

1 Introduction

Tropical cyclones (TCs) can cause severe natural disasters that are directly connected with the TC intensity. As a typical air–sea coupled system, TC development is affected by three kinds of physical processes: the atmospheric environmental conditions, TC internal dynamics, and the underlying boundary conditions (Chen and Ding, 1979; Emanuel et al., 2004). Among these, the underlying ocean conditions, such as a warm high sea surface temperature (SST) (Lavender et al., 2018; Schade, 2000; Sun et al., 2016, 2017a, b, 2019) and the presence of a sufficiently deep mixed layer (Jaimes et al., 2011; Shay et al., 2000; Wu et al., 2018; Yablonsky and Ginis, 2012; Yan et al., 2017; Zhao and Chan, 2017), have attracted considerable research attention. As a TC moves over ocean waters, TC intensification is determined by the balance of positive and negative feedback between the TC and the ocean. The positive feedback mechanism denotes that the strong winds during TCs increase the available latent heat for TC intensification, which is also known as the wind-induced-surface-heat-exchange (WISHE) theory (Emanuel, 1986; Jaimes et al., 2016; Riehl, 1950). At the same time, the strong winds induce strong mixing in the mixing layer, which creates ocean surface cooling and further inhibits the latent heat release (Chan et al., 2001; Lin et al., 2005; Schade and Emanuel, 1999), and is thus a negative feedback mechanism. Previous studies have suggested that an SST increase of 1°C could intensify a TC by 3–20 hPa of the minimum sea level pressure (MSLP) at the TC center (Emanuel, 1988; Evans, 1993; Schade and Emanuel, 1999; Sun et al., 2013, 2016; Wu et al., 2005). In addition, the subsurface ocean

Foundation item: The National Natural Science Foundation of China under contract No. 41706034; the Basic Scientific Fund for National Public Research Institutes of China under contract No. 2020Q05; the Open Fund of the Key Laboratory of Ocean Circulation and Waves, Chinese Academy of Sciences under contract Nos KLOCW1803 and KLOCW1804; the Open Fund of the Laboratory for Regional Oceanography and Numerical Modeling, Qingdao National Laboratory for Marine Science and Technology under contract No. 2019A02; the National Natural Science Foundation of China under contract Nos 91428206 and 41376038; the National Science and Technology Major Project under contract No. 2016ZX05057015; the National Programme on Global Change and Air-Sea Interaction under contract Nos GASI-03-01-01-02 and GASI-IPOVAI-01-05; the NSFC-Shandong Joint Fund for Marine Science Research Centers under contract No. U1606405.
*Corresponding author, E-mail: wghocean@yahoo.com

warm water benefits TC intensification by efficiently suppressing TC-induced SST cooling (Lin et al., 2005, 2009, 2013, 2014; Shay, 2010; Jaimes and Shay, 2015; Yablonsky and Ginis, 2012). Shay (2009) showed that TC intensification was directly correlated to large values of the 26°C isotherm depth and upper ocean heat content, which were helpful in predicting TC intensity with better estimates (Mainelli et al., 2008; Shay and Brewster, 2010). Thus, conditions of the oceanic environment are critical in TC development.

The ocean mesoscale eddy (OME) is an important ocean phenomenon and covers 20%–30% of the ocean area (Chaigneau et al., 2009; Chelton et al., 2011; Cheng et al., 2014; Lumpkin, 2016). The OME comprises a particular circulation system that modulates the subsurface thermocline, influencing ocean water temperature at the sea surface and also in the subsurface layers (Yang et al., 2013, 2015; Dong et al., 2014). In an investigation of ocean water temperature affected by warm OMEs (WOMEs) using the Argo dataset (Dong et al., 2014), the warm anomaly caused by WOMEs reached 1.4°C at the surface and 2.5°C at a depth of 370 m, with which the profiles of warm anomaly caused by WOMEs in the northwestern subtropical Pacific Ocean and southeastern tropical Indian Ocean were similar (Yang et al., 2013, 2015). Specific warm ocean conditions lead WOMEs to play a vital role in air–sea interactions (Anandh et al., 2020; Frenger et al., 2013; Jaimes et al., 2016), and are important in TC development (Shay, 2010). Moreover, the regions in which WOMEs have been observed are consistent with those of TCs, and most of the recorded TCs have encountered WOMEs (Ma et al., 2017). Under these circumstances, issues regarding the role of WOMEs on the track of TCs in TC development have been frequently studied, such as in Hurricane Opal (Hong et al., 2000; Shay et al., 2000), Hurricane Issac (Jaimes and Shay, 2015), Hurricane Katrina (Wu et al., 2007), Typhoon Maemi (Lin et al., 2005), and Typhoon Rammasun (Sun et al., 2016). These studies have focused on TC intensification and the strong TC intensity induced by a WOME located along the TC track. Both numerical experiments and observations have suggested that the warm anomalies of the upper ocean caused by WOMEs could reduce TC-induced SST cooling by limiting the negative feedback, and this warmer SST during the TC period would then enhance the heat fluxes transported to the TC (Wu et al., 2007; Jaimes et al., 2016), leading to enhanced TC intensity. However, few studies have considered the effect of WOME on TC intensity changes for those WOMEs positioned far away from the TC center. Based on previous studies (Frenger et al., 2013; Sun et al., 2016), the warm water in a WOME induced increased heat fluxes and a low local atmospheric pressure anomaly, which could change the atmospheric circulation of the TC. Through idealized experiments, in which a ring-shaped positive SST anomaly (SSTA) was added and centered on the TC center, Sun et al. (2014) found that the positive SSTA enhanced the TC within an effective radius and weakened it outside of that radius. This effect was explained by changes in atmospheric conditions (Sun et al., 2014). Although the ring-shaped SSTA did not reflect WOME accurately, both in shape and range, the study by Sun et al. (2014) was valuable in terms of how to investigate how TC intensity would change in response to WOME at varying locations with respect to the TC center. According to these results, it may be expected that a WOME in an outer area may have a different effect on TC intensity compared with a WOME located on the TC track. However, no studies have been conducted on this topic to our knowledge. Moreover, identification of the ranges in TC intensity changes on the spatial distribution of the WOME and the internal mechanisms remain unclear, and thus warrant further investigation.

In the present study, the response of TC intensity to a WOME positioned at varying locations with respect to the TC center is investigated through a series of idealized numerical simulations. In addition, the detailed spatial-temporal patterns of TC intensity change caused by the WOME at varying locations are studied. These results will be valuable in understanding the influence of complex ocean environments on TC development and will help to promote TC intensity forecasting skills. The remainder of this paper is presented as follows. The model and experimental design are introduced in Section 2. The changes in the TC intensity caused by a WOME at varying locations and the mechanisms are identified in Section 3. Finally, a discussion and conclusion are presented in Section 4.

2 Model and experimental design

2.1 *WRF-only experiments*

The Weather Research and Forecasting (WRF, version 3.5.1) model is a fully compressible, non-hydrostatic, terrain-following model (Skamarock et al., 2008), which was used for the investigation of TC intensity changes to the spatial distribution of WOMEs in the present study. The simulations were designed as a stationary TC forced by different SST conditions, including a control run (ExpAC) and 121 sensitivity experiments. The control run was conducted with spatially homogeneous SST conditions, which remained constant at 28.0°C. The sensitivity experiments were run with one WOME at varying locations with respect to the TC center. The initial TC wind field was provided by the WRF idealized TC module (Jordan, 1958; Rotunno and Emanuel, 1987), which was an axially symmetric cyclonic wind field at the center of the simulation area, covering an area within a radius of 412.5 km. The radius of the TC maximum wind speed (MWS) was 82.5 km, and the MWS was 15 m/s in the bottom layer, decreasing linearly to the top layer of the model. The simulation was integrated for 96 h on an f-plane where the Coriolis parameter f was 5.0×10^{-5}, and the simulation domain covered an area of 3 000 km× 3 000 km with a 9 km×9 km horizontal resolution and 38 vertical layers. Periodic, symmetric, and open radiative lateral boundary conditions were adopted in the simulation. The surface layer and planetary boundary layer parameterization schemes employed in the WRF model were the MM5 similarity scheme (Jiménez et al., 2012) and the Yonsei University scheme (Hong and Lim, 2006), respectively, which adopted the COARE formula for the exchange coefficients of momentum, heat, and moisture.

Figure 1 displays the results of the TC evolution from the control run. The simulated TC intensified steadily after the 24-h spin-up period, with the MWS increasing and the MSLP decreasing. By the end of 96 h, the MWS reached 49.7 m/s and the MSLP decrease was 55.0 hPa (Fig. 1a). The simulated azimuthal-mean TC structures of the intensification stage (48–96 h) were similar to real TCs and are shown in Figs 1b–f. The radius of the MWS was 40 km, where the maximum values of the tangential and vertical components of the wind speed were found (Figs 1b and d). The inflow winds (Fig. 1c) were located at 0–10 km in height, and the maximum values were found at 30–240 km from the TC center in the bottom layers, matching well with the location of the updrafts (Fig. 1d). Distinct downdrafts were found in the inner TC eyewall (0–30 km from the TC center) and at the outer areas (200–400 km from the TC center) (Fig. 1d). There was a warm core around the TC center at 3–15 km height, where strong potential vorticity occurred (Figs 1e and f). These features are consistent with both observations and previous model results (Wang,

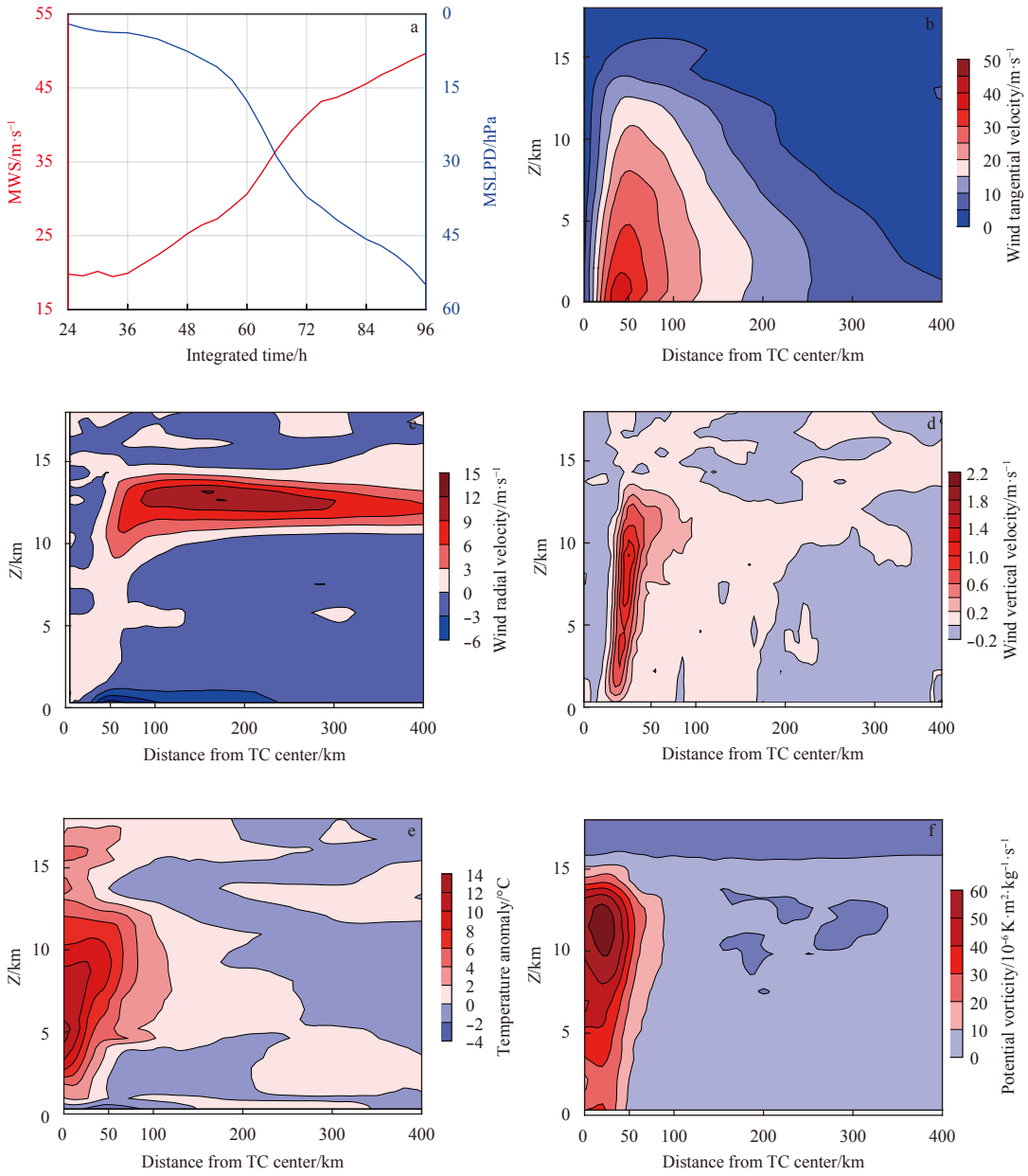

Fig. 1. Results of the control run presented as the simulated MWS and MSLP decrease (MSLPD) (a) and the azimuthal-mean vertical profiles of the tangential velocity (b), the radial velocity (c), the vertical velocity (d), the temperature anomaly (e), and the potential vorticity (f).

2009). Therefore, the same model settings were used for further sensitivity studies.

Previous studies have shown that TC intensity is affected by WOME (Hong et al., 2000; Lin et al., 2005; Shay et al., 2000; Wu et al., 2007); however, it remains unknown how TC intensity changes with the spatial distribution of WOME. To address this issue, we carried out a series of sensitivity experiments based on the control run by adding a WOME at various different locations while keeping the other entire model configurations unchanged. Since the effect of the ocean on TC was connected with the TC wind field according to the WISHE theory (Emanuel, 1986), WOME was primarily added inside the TC-influencing area in the sensitivity experiments. Moreover, it was essential to set a sufficiently fine spatial resolution to add the WOME in the sensitivity experiment to reveal the response of the TC intensity to the spatial distribution of the WOME. Therefore, the initial wind field (412.5 km radius) was covered with 11×11 grids centered on the initial TC center and a WOME centered on each grid point was added in the 121 sensitivity experiments (Fig. 2). The resultant grid resolution of the WOME locations was 82.5 km, which was equal to the initial radius of the TC MWS. In the present study, it was assumed that the circular positive SSTA played a similar role to that of a WOME in changing the TC intensity to express the effect of the WOME in the atmosphere-only model (Shan and Dong, 2019). Previous studies have shown that sea water temperature increases induced by WOMEs varied from 1.4°C to 2.5°C in the upper ocean layer (Dong et al., 2014; Zhang et al., 2014) and that WOME radius distribution was close to the Gaussian distri-

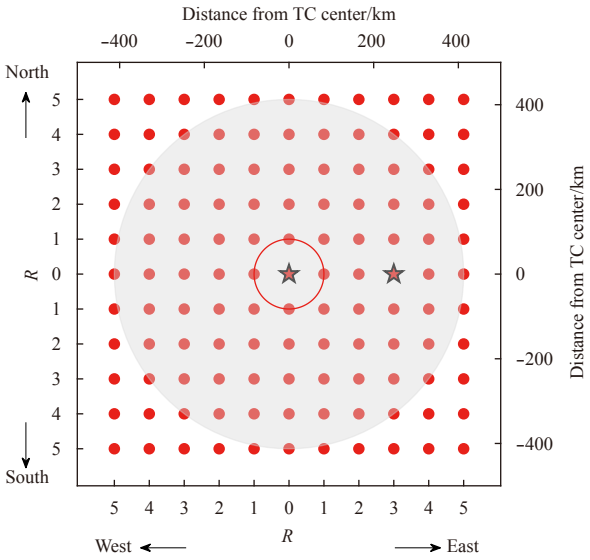

Fig. 2. Centers of the WOME in sensitivity experiments (red dots and stars denote the centers of the WOME in 121 WRF-only sensitivity experiments and 2 WRF-3DPWP coupled sensitivity experiments, respectively; and gray shadow and red circle denote the areas of the initial TC wind field and the WOME at the TC center, respectively).

bution, where the peak value appeared at 80 km and the mean radius was 86 km (Cheng et al., 2014). Therefore, it was reasonable to set the amplitude of the circular SSTA to 2.0°C and the WOME radius as 82.5 km in the current study. Hereafter, R is used to represent this 82.5 km radius. Based on these experimental settings, in the 121 sensitivity experiments, WOME at the TC center influenced all of the TC updraft areas, and that at 1R influenced part of the updraft areas. WOME at distances over 2R primarily influenced the outer areas of the TC and had little direct effect on the updraft areas. The response of the TC intensity to WOME at varying locations was investigated in the 121 sensitivity experiments.

2.2 *WRF-3DPWP coupled experiments*

To reveal how an actual WOME affects TC development at various locations, three more experiments were conducted using an atmosphere–ocean coupled model. The coupled model in the present study consisted of WRF and the three-dimensional Price-Weller-Pinkel (3DPWP) ocean circulation model (Price, 1981; Price et al., 1994; Skamarock et al., 2008). The 3DPWP model solved for the wind-driven and baroclinic ocean response, including vertical advection/upwelling, entrainment/mixing, horizontal advection, and the pressure gradient force. In this model, the surface mixed layer was evolved via entrainment mixing and air–sea exchanges. The bulk transfer coefficient for the sensible heat flux (SHF) and the latent heat flux (LHF) was 1.3×10^3. The momentum flux was calculated using the bulk transfer formula. The drag coefficient was given by Powell et al. (2003). The ocean model shared the same domain and grid as the WRF model and was coupled with WRF every minute, using the surface stress and heat and moisture fluxes and passing the SST back to the atmospheric model. Thirty ocean layers in the vertical were set at 5, 15, 25, 35, 45, 55, 65, 75, 85, 95, 105, 115, 125, 135, 145, 155, 165, 175, 185, 195, 210, 230, 250, 270, 290, 310, 330, 350, 370, and 390 m. The initial vertical profiles of ocean temperature and salinity were taken from the World Ocean Atlas 2018 (WOA18) (Locarnini et al., 2018; Zweng et al., 2018) seasonal-mean temperature and salinity data, following the method from Lu et al. (2016).

The initial conditions and parameterizations in the atmosphere model employed in the WRF-3DPWP coupled experiments were the same as those in the WRF-only experiments. Three experiments were carried out (Table 1). The first was conducted using the WOA18 vertical profiles of sea water temperature and salinity, which were horizontally uniform in all the ocean layers within the 3DPWP model (henceforth ExpCC), eliminating the influence of WOMEs. The sea temperature and salinity profiles are shown in Fig. 3. The other two experiments were run using a circular and axially symmetric WOME in the inner and outer areas of the TC. The inner one was placed at the center of the initial TC field (henceforth Exp0R), and the outer one was placed at 3R east of TC center (henceforth Exp3R). The positions of the WOME in Exp0R and Exp3R are shown in Fig. 2. The structure of the WOME was according to Zhang et al. (2013), and the temperature and salinity were set to be uniform above 100 m in depth to enhance the effect of the WOME on TC. The maximum ocean temperature anomaly was +2.0°C, consistent with the WRF-only experiments. The outer radius of the WOME was 100 km, comparable with R. The ocean temperature profiles from ExpCC, Exp0R, and Exp3R are shown in Figs 3b–d. The WOME added into the horizontally uniform ocean condition broke the initial oceanic equilibrium but the resulting change of the upper ocean thermal structure from the self-adjustment of the ocean model was much smaller than that caused by the storm forcing (figure not shown), indicating that this disturbance caused by the insertion of the WOME is negligible.

3 Results

3.1 *Changes in the TC intensity in response to the WOME distribution*

Figure 4 shows the simulated TC intensities in the WRF-only control run and the 121 sensitivity experiments and their differences to the control run. During the first 60 h, the changes in the simulated TC intensities were related to the spatial distribution of the WOME relative to the TC center (Figs 3a–b). The TC intensity increased when a WOME was within 2R but weakened when the WOME was beyond 2R. In experiments within 2R, the MWS (Fig. 4a) and MSLP (Fig. 4b) were approximately 2–10 m/s higher and 5–20 hPa lower than those in the control run, respectively. The MWS and MSLP decreased and increased by 2–5 m/s and 2–7 hPa, respectively, in experiments at 2R–5R. After 60 h, most TC intens-

Table 1. Configuration of the WRF-3DPWP coupled experiments

Experiment	Description
ExpAC	control run of the WRF-only experiments using an atmosphere-only model
ExpCC	control run of the coupled experiments with horizontally uniform temperature/salinity conditions in the ocean model and the same settings of the atmosphere model as ExpAC
Exp0R	a WOME was placed at TC center (other conditions the same as ExpCC)
Exp3R	a WOME was placed at 3R east of TC center (other conditions the same as ExpCC)

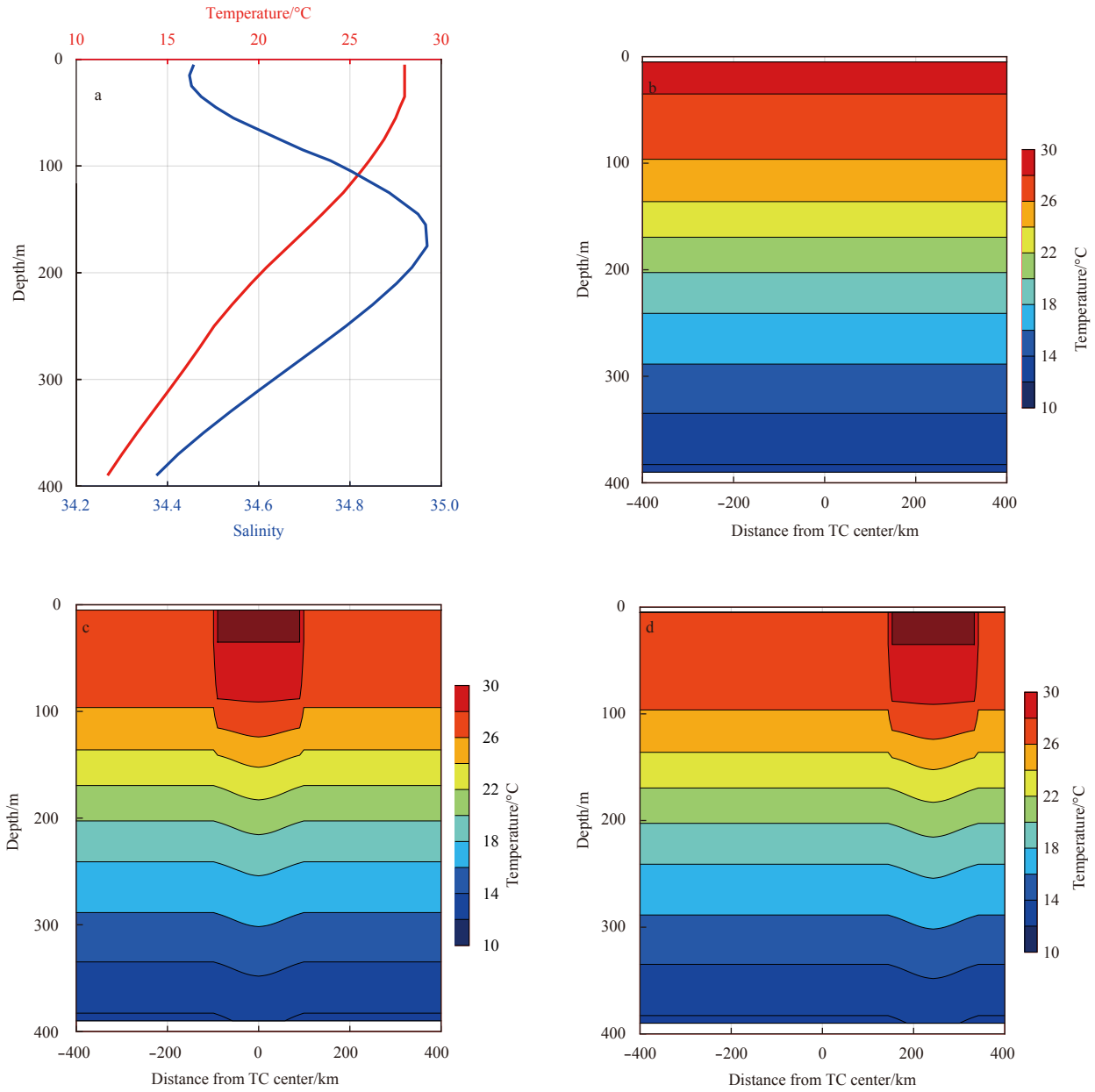

Fig. 3. Vertical profiles of the sea temperature (red line) and salinity (blue line) in 3DPWP model (a) and the initial zonal transections of the sea temperature across the TC center in ExpCC (b), Exp0R (c) and Exp3R (d), respectively.

ities weakened in experiments outside 1*R*. The maximum weakening was up to 10 m/s and 20 hPa for the MWS and MSLP, respectively. It should be noted that the amplitude of the TC intensification caused by the WOME at the TC center declined with increasing integration. This may have been the result of the decreasing percentage of the energy provided by the WOME in the total energy transformed to TC kinetic energy.

For more distinct spatial patterns of the TC intensity changes corresponding to the WOME at varying locations, the differences in the TC intensity between sensitivity experiments and the control run were spatially interpolated into polar coordinates centered on the TC center using the daily mean results (Figs 4c–e). During the simulation, TC intensity exhibited opposite responses to the WOME in inner and outer areas relative to the TC center, and the range of the inner area decreased with continued simulation. During 24–48 h (Fig. 4c), TCs were distinctly intensified with a WOME at the TC center and 1*R*–2*R*. The MWS was 8, 4–8, and 0–4 m/s stronger than that in the control run when a WOME was at the TC center, 0–1*R*, and 1*R*–2*R*, respectively. The simulated intensities were weakened by 0–2 m/s if a WOME was at 3*R*–5*R*. For 48–72 h (Fig. 4d), the weakening effect of the WOME in the outer area became pronounced. All WOMEs at 2*R*–5*R* weakened the simulated TC intensities by 1–5 m/s. The maximum weakening reached 5 m/s and occurred when WOME was at 3*R*. The strengthening effect decreased to 0–6 m/s when the WOME was at the TC center and 1*R*. For 72–96 h (Fig. 4e), the WOME at all the other locations besides the TC center depressed the TC intensification. The strongest decline reached 10 m/s at 2*R*–3*R*. A WOME could intensify the simulated TC intensity only when located at the TC center. It was noted that the opposite changes of TC intensity to WOMEs within and outside 2*R* were distinct before 60 h and the strongest strengthening and weakening oc-

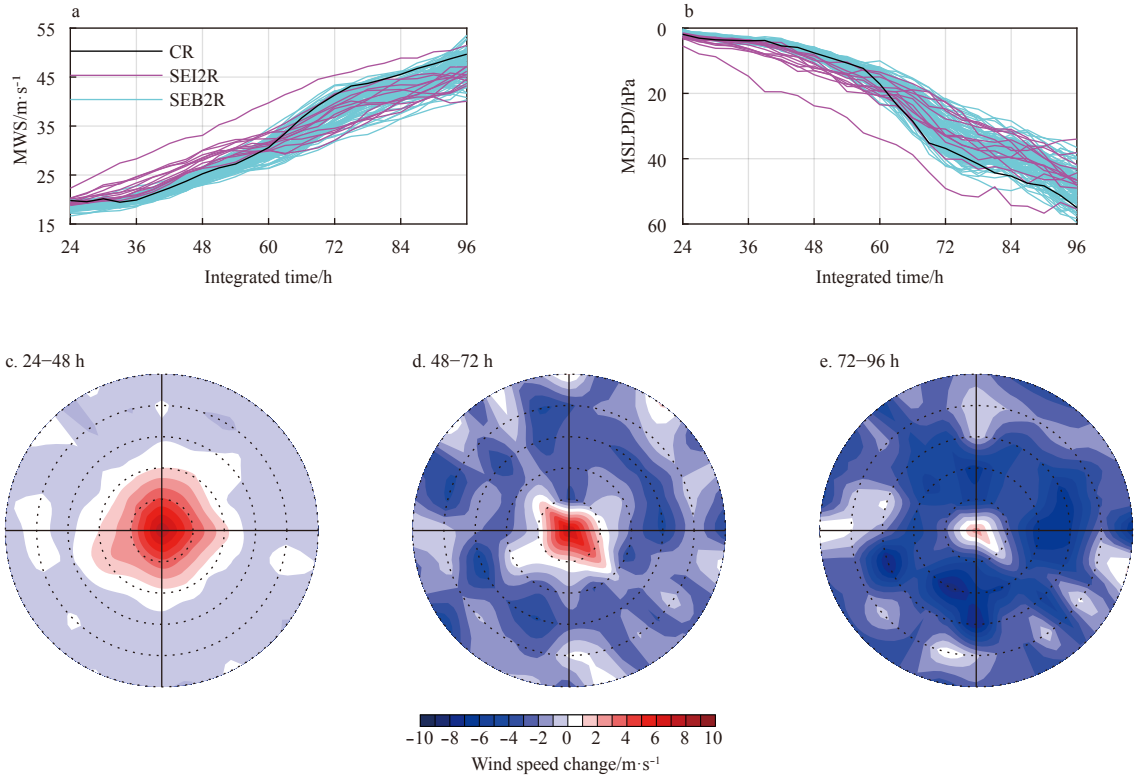

Fig. 4. Simulated MWS at 10-m height (a) and MSLP decrease (MSLPD) (b) in the control run (CR) and sensitivity experiments in which WOME was within (SEI2R) and beyond 2*R* (SEB2R), and the mean differences of the MWS between the sensitivity experiments and the control run at varying WOME locations at 24–48 h (c), 48–72 h (d), and 72–96 h (e) (black circles indicate ranges 1*R*–5*R*).

curred with WOMEs located at the TC center and at 3*R*, respectively. Therefore, the experiments in which WOMEs were located at the TC center and at 3*R* were selected and the mean results at 24–60 h were used for further investigation and a mechanistic analysis.

Figures 5a and b reveal the change in the surface wind fields averaged over 24–60 h for WOME at the TC center and at 3*R*, respectively. For the WOME at the TC center, wind speed increased within a 200-km radius, and the maximum increase reached 21.2 m/s at radii of approximately 30–50 km. For the WOME at 3*R*, the TC wind speed dramatically decreased and the maximum decrease reached 9.7 m/s at approximately 50 km from the TC center.

The TC precipitation also revealed the different influence of WOME at varying locations to the TC center. It was found that the TC precipitation in the control run was primarily within 100 km to the TC center, although there was some precipitation beyond this range (Fig. 6a). In contrast, the WOME at the TC center and 3*R* produced very different results. For the former, the TC rainband was better organized and more concentrated to the smaller TC eye (~20 km), and the maximum precipitation was found at 50–100 km to the TC center (Fig. 6b). For the latter, the TC rainband expanded to beyond 200 km to the TC center, and the maximum precipitation was outside 100 km to the TC center (Fig. 6c).

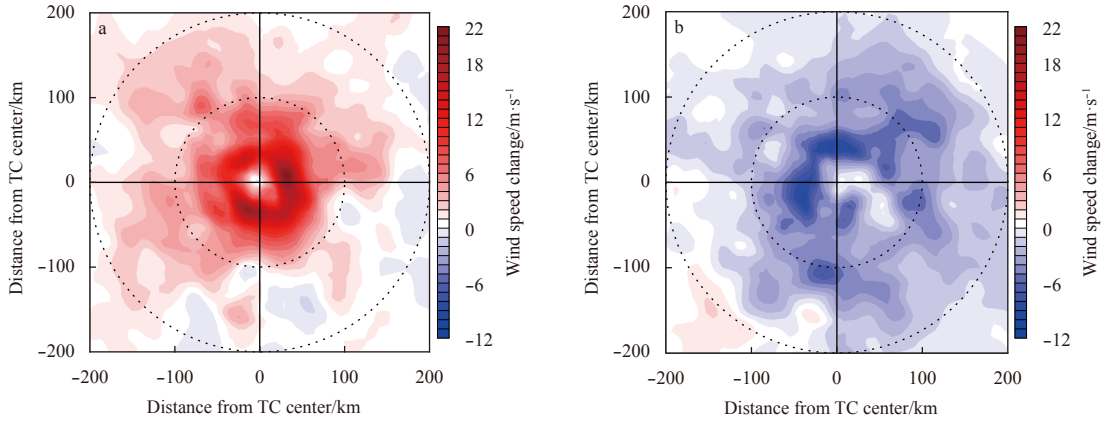

Fig. 5. Spatial difference of the surface wind speed in the sensitivity experiments compared to the control run: WOME at the TC center (a) and at 3*R* (b).

Development of the outer spiral rainband depressed the TC intensification (Shapiro, 1982; Willoughby et al., 1984; Mathur, 1998; Wang, 2002, 2009); thus, the change in the rainband structure again suggested that the TC intensity was closely related to the WOME location.

The differences in the vertical structure of the TC wind during 24–60 h caused by the WOME at the TC center and 1*R*–5*R* were further evaluated and are displayed in Fig. 7. In the control run, the TC MWS decreased from 22.5 m/s in the bottom layer to 0.7 m/s in the top layer (figure not shown). The results revealed that the WOME within and outside 2*R* to the TC center strengthened and weakened the TC MWS from the surface to the outflow layers (~13 km height), respectively. Wind speed at the bottom layer increased 12.3, 3.6, and 0.7 m/s when the WOME

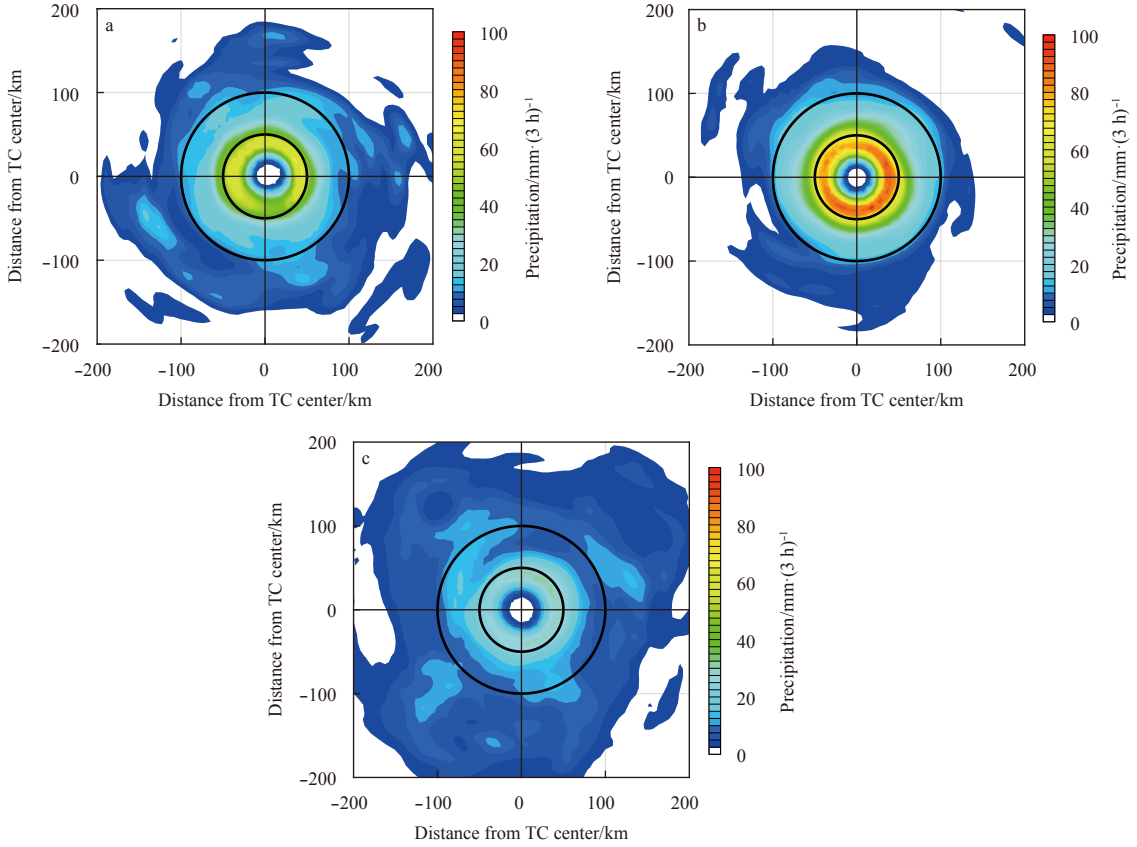

Fig. 6. Results of the average TC precipitation in control run (a) and sensitivity experiments in which the WOME was at the TC center (b) and at 3*R* (c).

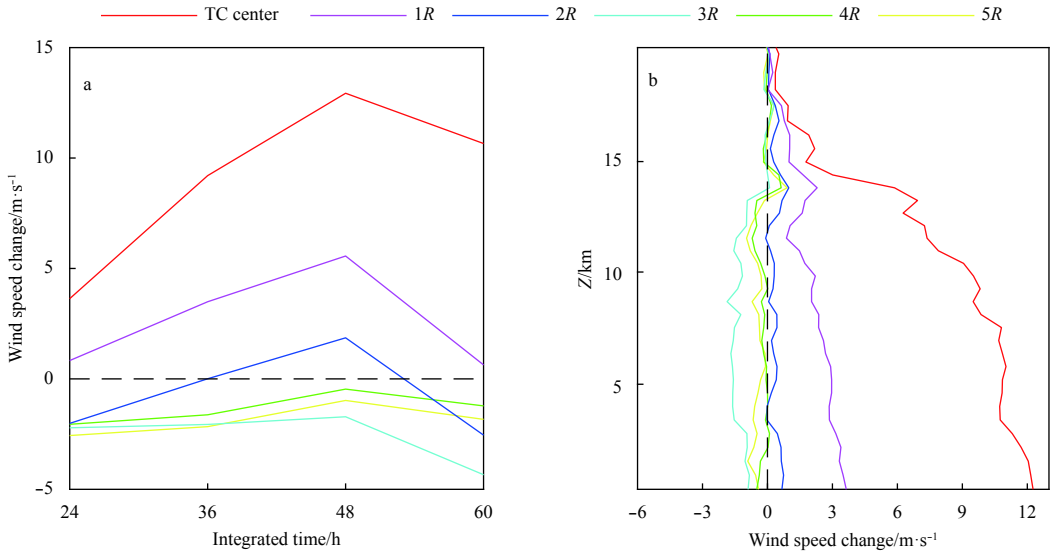

Fig. 7. Differences in the surface wind speed in the sensitivity experiments (a) and the vertical profiles of the maximum azimuthal-mean wind speed as compared to the control run during 24–60 h (b).

was at the TC center, 1*R*, and 2*R*, respectively (Fig. 7a). Changes in all the other vertical layers were positive, indicating that the TC secondary circulation was increased by the WOME in these areas. As the WOME was at 3*R*–5*R* to the TC center, the wind speeds at the bottom layer decreased by –0.9, –0.5, and –0.41 m/s, respectively, and wind speeds decreased in layers below 13-km in height. These results also confirmed that the WOME at the TC center and at 3*R* played the strongest strengthening and weakening effect on the TC intensity. Thus, the mean results of the experiments in which the WOMEs were located at the TC center and at 3*R* at 24–60 h were used for further mechanistic analysis.

3.2 *Mechanisms of the WOME that influence the TC intensity*

The TC intensity change is linked to heat energy drawn from the ocean in the form of the SHF and LHF, which are transported and transformed by the secondary circulation (Emanuel, 1986; Riemer et al., 2010). In general, a WOME produces localized low pressure and updraft anomalies, causing convergence of the wind field centering on the WOME, thereby inducing further changes in the atmospheric circulation. Figure 8 shows the average changes in the secondary circulation caused by the WOME at the TC center and at 3*R* during 24–60 h compared with the control run. For a WOME at the TC center, the secondary circulation was enhanced by 3.0, 0.7, and 8.5 m/s in the inflow, updraft, and outflow areas, respectively (Fig. 8a). Inflow increased primarily at 30–200 km to the TC center in the lower layers. The updraft increased within 50 km, and the eyewall become narrower. These results expressed that the TC structure was more organized with the WOME at TC center. For a WOME at 3*R*, the secondary circulation was weakened by 3.1, 0.4, and 2.8 m/s in the inflow, updraft, and outflow areas, respectively (Fig. 8b). The weakening of inflow caused by the WOME at 3*R* was primarily at 30–200 km to the TC center in the lower layers. The updraft decreased near the original TC eyewall and increased by 0.1–0.2 m/s at approximately 70 km from the TC center, indicating an expansion of the TC eye. The outflow weakened and descended from 13 to 9 km in height. The TC structure was much less organized compared with the control run.

Figure 9 shows the average changes in the SHF and LHF caused by the WOME at the TC center and at 3*R* during 24–60 h. Both the SHF and LHF increased within a radius of 100 km when the WOME was at the TC center (Figs 9a and c), and the maximum increases were over 257 and 817 W/m^2, respectively, indicating that the ocean released more heat energy to the TC. The additional heat energy input to the TC was then transformed into the kinetic energy of the TC by the enhanced secondary circulation, strengthening the TC intensity. In the experiment with the WOME at 3*R*, the WOME decreased the inflow and consequently decreased the heat energy transported by the inflow (Figs 9b and d). The reduced heat energy input to the TC weakened its intensity and further decreased the SHF and LHF according to the WISHE theory. On average, the SHF and LHF decreased by 94 and 248 W/m^2, respectively (Figs 9b and d). The SHF and LHF were also integrated within 30–100 and 30–200 km from the TC center (Table 2), which were the main heat energy sources of the TC. The total SHF increased by 2.8×10^6 and 4.5×10^6 W within a radii of 30–100 and 30–200 km, respectively, when a WOME was located at the TC center. Total increases in the LHF were 1.1×10^7 and 2.1×10^7 W within a radius of 30–100 and 30–200 km, respectively. In contrast, both the SHF and LHF decreased when the WOME was located at 3*R*. The SHF and LHF decreased by 6.7×10^5 and 1.9×10^6 W within radii of 30–100 km, respectively, and by 1.1×10^6 and 3.8×10^6 W within a radii of 30–200 km, respectively.

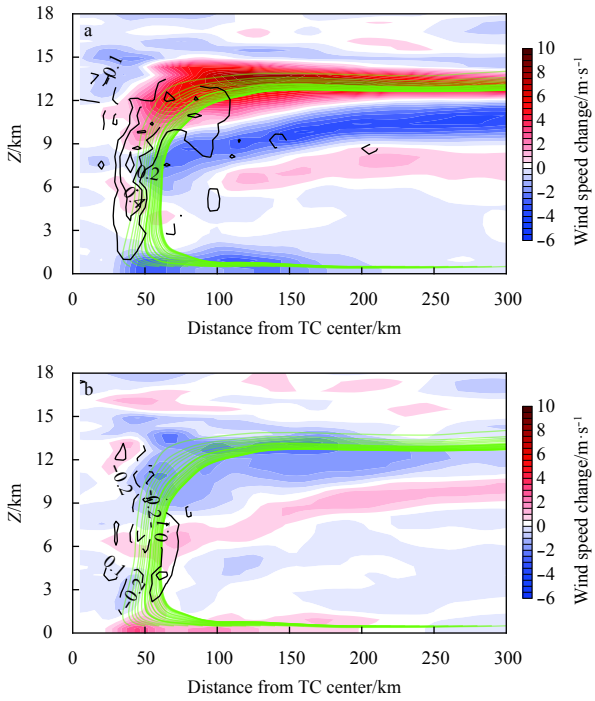

Fig. 8. Results of the azimuthal-mean and radial-vertical profile of the TC wind speed (the color denotes radial wind speed; green and black solid and dashed lines denote the streamlines of the control run and the positive and negative updraft anomalies, respectively), presented as the WOME at the TC center (a) and at 3*R* (b).

In conclusion, more heat energy was transferred to the TC from the ocean when the WOME was located in the inner area, strengthening the TC intensity. Heat energy drawn from the ocean for the TC was impeded by the presence of the WOME in the outer area, which weakened the TC intensity.

Because the air–sea interaction is important for TC intensification (Halliwell et al., 2011; Lee and Chen, 2014; Wu et al., 2016), the vertical ocean structure was vital in the TC simulation (Wadler et al., 2018). Thus, a coupled model was run to further examine the response of the TC intensity to the WOME location. Three experiments were executed (i.e., ExpCC, Exp0R and Exp3R, Table 1) and the simulated TC intensities and heat fluxes (SHF plus LHF) are shown in Fig. 10. The TC intensity was much weaker if coupled with an ocean model after 63 h. The maximum MSLP decrease attained 55 hPa in the control run of the WRF-only experiments (i.e., ExpAC), whereas the value was only 26 hPa after coupling (i.e., in ExpCC) (Fig. 10a). It should be noted that the TC intensity from ExpCC was stronger than that without coupling (i.e., ExpAC) before 63 h. This was because the solar radiation warmed the SST in the daytime (figure not shown), which induced more heat fluxes and provided more heat energy to the TC because the simulation began at midnight (Fig. 10b). After 72 h, the simulated TC intensity of ExpCC reduced as a result of SST cooling (Figs 11a–d). The response of the TC intensity to a WOME at the outer and inner area of the TC in the coupled model was very similar to that in the WRF-only experiments. For the WOME at the TC center, the simulated TC intensified rapidly during 24–48 h and was maintained before 66 h. It was noted that the TC intensified again after 84 h, and the maximum MSLP decrease attained 41 hPa at 96 h. The TC intensity

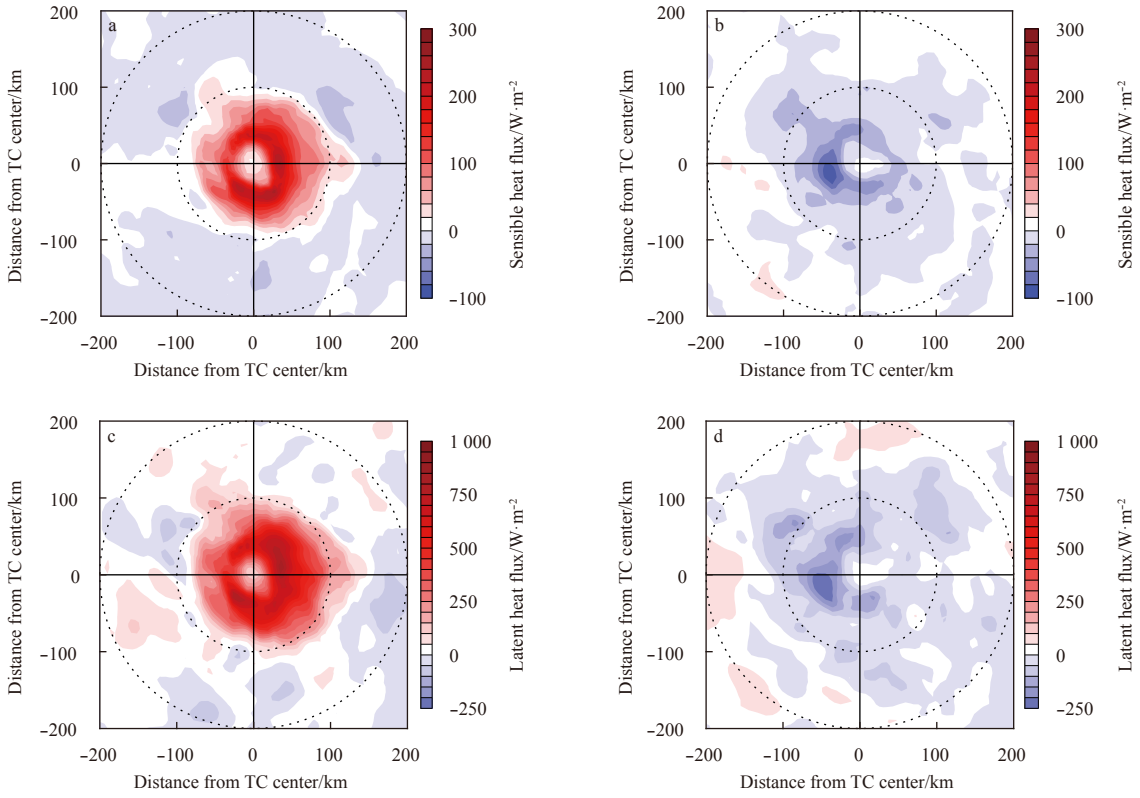

Fig. 9. Spatial differences in the SHF (a, b) and the LHF (c, d) from the sensitivity experiments compared with the control run presented with the WOME at the TC center (a, c) and 3*R* (b, d).

Table 2. Integrated changes of SHF and LHF caused by WOME

WOME location		30–100 km	30–200 km
TC center	SHF/W	2.8×10^6	4.5×10^6
	LHF/W	1.1×10^7	2.1×10^7
3*R*	SHF/W	-6.7×10^5	-1.1×10^6
	LHF/W	-1.9×10^6	-3.8×10^6

from Exp0R was stronger than that in ExpCC throughout the entire integration since the WOME provided more heat fluxes (312 W/m² on average for the whole period) to the TC. As the WOME was at 3*R*, the WOME weakened the secondary circulation and reduced the heat fluxes by 20–150 W/m² during the simulation. As a result, the TC intensity was weaker than the control run prior to 75 h. The TC intensities of the first 75 h from the coupled model confirmed the result in the WRF-only experiments. Unlike the atmosphere-only experiments, the TC was stronger in Exp3R than that in ExpCC after 75 h and the TC intensified again after 81 h in Exp0R. These differences were investigated with the inclusion of ocean responses in the coupled experiments, including ocean water temperature at a depth of 5-m and a temperature zonal transection across the TC center (Fig. 11).

Figure 11 shows the changes of the upper ocean thermal structure. When developing over a horizontally homogeneous ocean (Figs 11a–d), the TC cooled the 0–50 m layer due to surface flux outside the TC eye where the surface wind speed was strong. The cooling areas of the surface layer expanded to ~200 km, and the maximum decrease was –1.8°C at 30 km to the TC center. TC-induced upwelling existed around the TC center and the cooling area was larger with increasing depth (Figs 11m–p). The

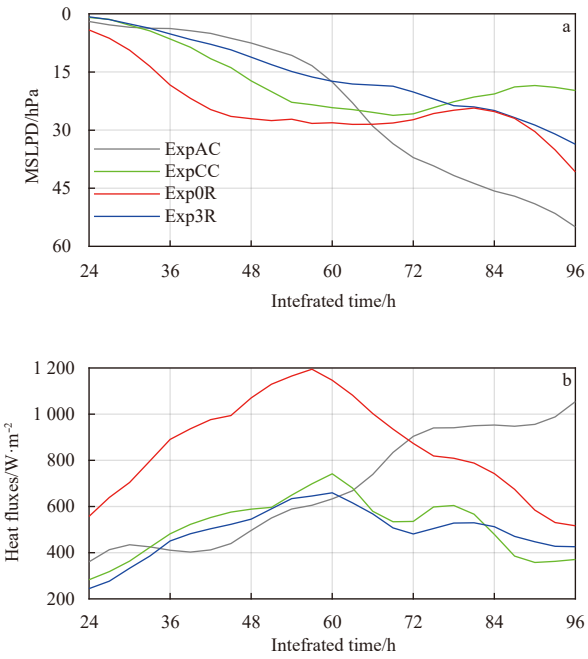

Fig. 10. Time series of the simulated TC intensities (a) and the mean heat fluxes within a radius of 100 km from the TC center drawing (b) from the control experiment using WRF-only atmosphere model (ExpAC), the control experiment using WRF-3DPWP coupled model (ExpCC), and the sensitivity experiments with WOME at the inner area (Exp0R) and at the outer area (Exp3R) using the WRF-3DPWP coupled model.

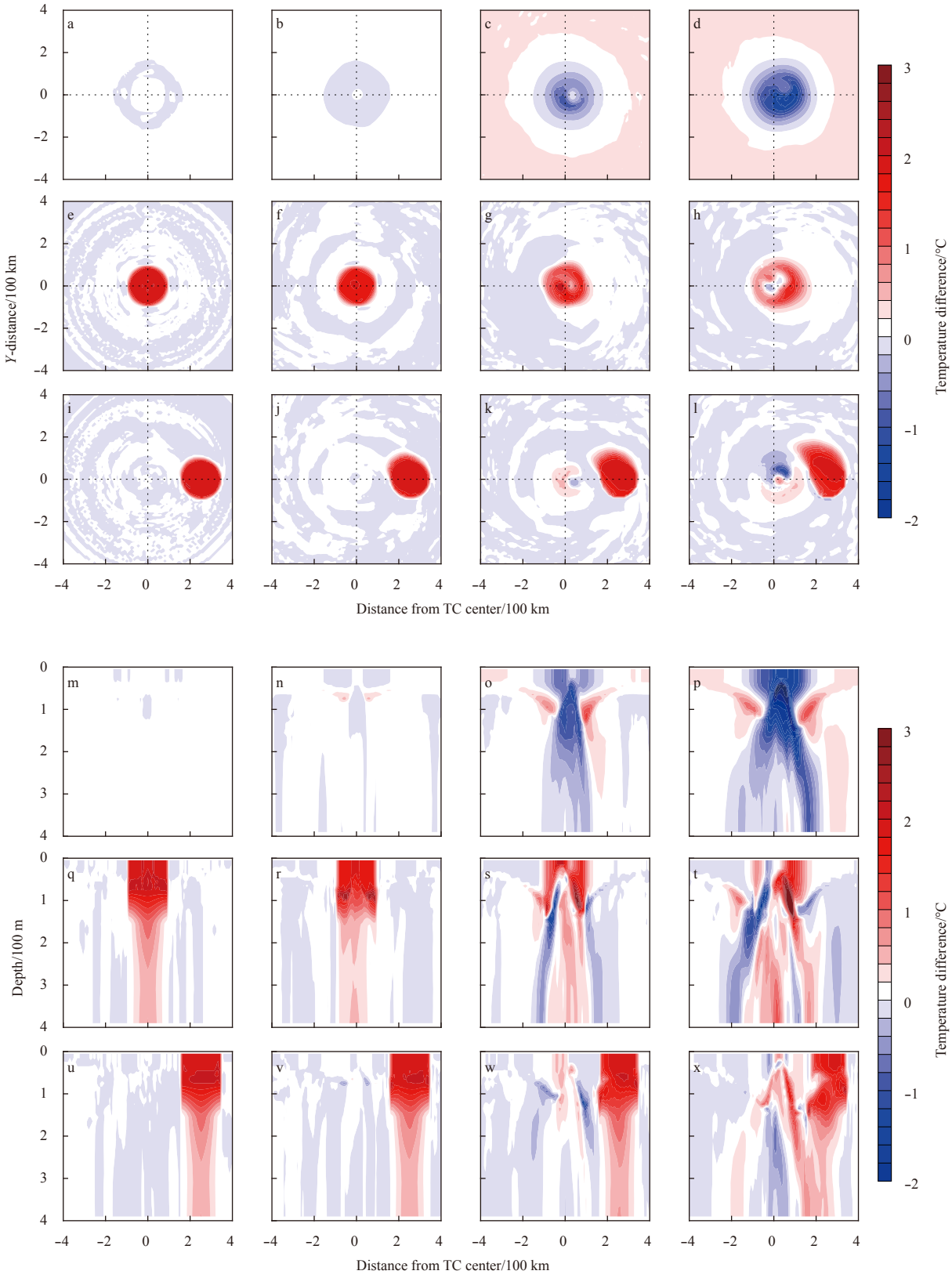

Fig. 11. Water temperature differences to the initial condition at a depth of 5 m of ExpCC (a–d) and the temperature differences of Exp0R (e–h) and Exp3R (i–l) to the control run across the TC center at 24 h (first column), 48 h (second column), 72 h (third column) and 96 h (fourth column); m–x are same as a–l but this shows the zonal transections in temperature differences.

water temperature decreased over 2.0°C at depths of 35–165 m, and the maximum cooling was at a depth of 55 m with –3.0°C. In addition, with the TC-induced cooling, the ocean water temperature increased outside 180 km in the mixed layer and the sub-

duction went toward the TC center. The maximum temperature increase was 1.3°C at a depth of 105 m and 170 km from the TC center. For Exp0R, the surface water was warmer than the control run within 100 km until 96 h (Figs 11e–h), which resulted in a stronger TC. Warm water at deeper layers was upwelled and the heat energy of the upper layers was replenished (Figs 11q–t). The re-intensification after 81 h may have been the result of a TC structure adjustment, TC energy redistribution, and continuous energy supplement from the ocean. For Exp3R, the surface warm water in the WOME at 3*R* was advected counterclockwise towards the TC center by the cyclonic TC wind (Figs 11i–l). Thus, water around the TC center became warmer than ExpCC from ~72 h. This also was a result of entrainment that occurred at the same time (Figs 11u–x). This warmer sea surface water was offset against the SST cooling around the TC center and provided more heat fluxes than that in ExpCC (Fig. 10b). This increased TC energy input and contributed to TC further intensification.

4 Discussion and conclusions

The response of TC intensity change to the spatial distribution of the WOME was investigated using two sets of idealized experiments using the WRF model and the WRF-3DPWP coupled model. This study detailed the spatial-temporal patterns of TC intensity change caused by the WOME at varying locations. The idealized simulation employed a stationary TC, and thus the results may only be applied to TCs with slow propagation that pass by several tandem WOMEs. Future research could further this investigation with the use of numerical simulations involving a series of real TC cases that passed by WOMEs at varying distances to the TC center.

The results of the present study showed opposite responses of TC intensity to a WOME located in the inner and outer TC areas. The TC was strongly intensified (weakened) with a WOME located in the inner (outer) TC area. More importantly, this study found that both the range of the inner (outer) area and amplitude of the TC intensity enhancement (weakening) caused by the WOME in the inner (outer) area decreased (increased) with time. Maximum weakening occurred when the WOME was positioned at 2–3*R*. The opposite effect of the WOME on TC intensity change in the inner and outer areas could be explained by WOME-induced changes of the TC secondary circulation and surface heat fluxes. A WOME located in the inner area caused a lower pressure and updraft anomaly, strengthened the secondary circulation, and increased the SHF and LHF transfer with the secondary circulation. The additional heat energy input to the TC subsequently enhanced the TC intensity. If WOME was positioned in the outer area, its induced secondary circulation change inhibited the transport of heat fluxes and depressed TC development. These results can deepen our understanding of how TCs interact with WOMEs and help to improve 48–72 h TC intensity forecast results using remote sensing data, thus further improving TC intensity forecasting.

References

Anandh T S, Das B K, Kuttippurath J, et al. 2020. A coupled model analyses on the interaction between oceanic eddies and tropical cyclones over the Bay of Bengal. Ocean Dynamics, 70(3): 327–337, doi: 10.1007/s10236-019-01330-x

Chaigneau A, Eldin G, Dewitte B. 2009. Eddy activity in the four major upwelling systems from satellite altimetry (1992–2007). Progress in Oceanography, 83(1–4): 117–123

Chan J C L, Duan Yihong, Shay L K. 2001. Tropical cyclone intensity change from a simple ocean–atmosphere coupled model. Journal of the Atmospheric Sciences, 58(2): 154–172, doi: 10.1175/1520-0469(2001)058<0154:TCICFA>2.0.CO;2

Chelton D B, Schlax M G, Samelson R M. 2011. Global observations of nonlinear mesoscale eddies. Progress in Oceanography, 91(2): 167–216, doi: 10.1016/j.pocean.2011.01.002

Chen Lianshou, Ding Yihui. 1979. An Introduction to the West Pacific Ocean Typhoons (in Chinese). Beijing: Science Press, 1–491

Cheng Y H, Ho C R, Zheng Quanan, et al. 2014. Statistical characteristics of mesoscale eddies in the north pacific derived from satellite altimetry. Remote Sensing, 6(6): 5164–5183, doi: 10.3390/rs6065164

Dong Changming, McWilliams J C, Liu Yu, et al. 2014. Global heat and salt transports by eddy movement. Nature Communications, 5(1): 3294, doi: 10.1038/ncomms4294

Emanuel K A. 1986. An air-sea interaction theory for tropical cyclones. Part I: steady-state maintenance. Journal of the Atmospheric Sciences, 43(6): 585–605, doi: 10.1175/1520-0469(1986)043<0585:AASITF>2.0.CO;2

Emanuel K A. 1988. The maximum intensity of hurricanes. Journal of the Atmospheric Sciences, 45(7): 1143–1155, doi: 10.1175/1520-0469(1988)045<1143:TMIOH>2.0.CO;2

Emanuel K, DesAutels C, Holloway C, et al. 2004. Environmental control of tropical cyclone intensity. Journal of the Atmospheric Sciences, 61(7): 843–858, doi: 10.1175/1520-0469(2004)061<0843:ECOTCI>2.0.CO;2

Evans J L. 1993. Sensitivity of tropical cyclone intensity to sea surface temperature. Journal of Climate, 6(6): 1133–1140, doi: 10.1175/1520-0442(1993)006<1133:SOTCIT>2.0.CO;2

Frenger I, Gruber N, Knutti R, et al. 2013. Imprint of southern ocean eddies on winds, clouds and rainfall. Nature Geoscience, 6(8): 608–612, doi: 10.1038/ngeo1863

Halliwell G R Jr, Shay L K, Brewster J K, et al. 2011. Evaluation and sensitivity analysis of an ocean model response to Hurricane Ivan. Monthly Weather Review, 139(3): 921–945, doi: 10.1175/2010MWR3104.1

Hong Xiaodong, Chang S W, Raman S, et al. 2000. The interaction between hurricane opal (1995) and a warm core ring in the Gulf of Mexico. Monthly Weather Review, 128(5): 1347–365, doi: 10.1175/1520-0493(2000)128<1347:TIBHOA>2.0.CO;2

Hong S Y, Lim J O J. 2006. The WRF single-moment 6-class microphysics scheme (WSM6). Asia-Pacific Journal of Atmospheric Sciences, 42(2): 129–151

Jaimes B, Shay L K. 2015. Enhanced wind-driven downwelling flow in warm oceanic eddy features during the intensification of Tropical Cyclone Isaac (2012): observations and theory. Journal of Physical Oceanography, 45(6): 1667–1689, doi: 10.1175/JPO-D-14-0176.1

Jaimes B, Shay L K, Brewster J K. 2016. Observed air-sea interactions in tropical cyclone Isaac over Loop Current mesoscale eddy features. Dynamics of Atmospheres and Oceans, 76: 306–324, doi: 10.1016/j.dynatmoce.2016.03.001

Jaimes B, Shay L K, Halliwell G R. 2011. The response of quasigeostrophic oceanic vortices to tropical cyclone forcing. Journal of Physical Oceanography, 41(10): 1965–1985, doi: 10.1175/JPO-D-11-06.1

Jiménez P A, Dudhia J, González-Rouco J F, et al. 2012. A revised scheme for the WRF surface layer formulation. Monthly Weather Review, 140(3): 898–918, doi: 10.1175/MWR-D-11-00056.1

Jordan C L. 1958. Mean soundings for the West Indies area. Journal of Meteorology, 15(1): 91–97, doi: 10.1175/1520-0469(1958)015<0091:MSFTWI>2.0.CO;2

Lavender S L, Hoeke R K, Abbs D J. 2018. The influence of sea surface temperature on the intensity and associated storm surge of tropical cyclone Yasi: a sensitivity study. Natural Hazards and Earth System Sciences, 18(3): 795–805, doi: 10.5194/nhess-18-795-2018

Lee C Y, Chen S S. 2014. Stable boundary layer and its impact on tropical cyclone structure in a coupled atmosphere-ocean model. Monthly Weather Review, 142(5): 1927–1944, doi: 10.1175/MWR-D-13-00122.1

Lin I I, Black P, Price J F, et al. 2013. An ocean coupling potential intensity index for tropical cyclones. Geophysical Research Let-

ters, 40(9): 1878–1882, doi: 10.1002/grl.50091
Lin I I, Pun I F, Wu C C. 2009. Upper-ocean thermal structure and the western North Pacific category 5 typhoons: Part II. dependence on translation speed. Monthly Weather Review, 137(11): 3744–3757, doi: 10.1175/2009MWR2713.1
Lin I I, Pun I F, Lien C C. 2014. "Category-6" supertyphoon Haiyan in global warming hiatus: Contribution from subsurface ocean warming. Geophysical Research Letters, 41(23): 8547–8553, doi: 10.1002/2014GL061281
Lin I I, Wu C C, Emanuel K A, et al. 2005. The interaction of supertyphoon Maemi (2003) with a warm ocean eddy. Monthly Weather Review, 133(9): 2635–2649, doi: 10.1175/MWR3005.1
Locarnini R A, Mishonov A V, Baranova O K, et al. 2018. World Ocean Atlas 2018, Volume 1: Temperature. NOAA Atlas NESDIS 81. US: NOAA, 52
Lu Zhumin, Wang Guihua, Shang Xiaodong. 2016. Response of a preexisting cyclonic ocean eddy to a typhoon. Journal of Physical Oceanography, 46(8): 2403–2410, doi: 10.1175/JPO-D-16-0040.1
Lumpkin R. 2016. Global characteristics of coherent vortices from surface drifter trajectories. Journal of Geophysical Research: Oceans, 121(2): 1306–1321, doi: 10.1002/2015JC011435
Ma Zhanhong, Fei Jianfang, Liu Lei, et al. 2017. An investigation of the influences of mesoscale ocean eddies on tropical cyclone intensities. Monthly Weather Review, 145(4): 1181–1201, doi: 10.1175/MWR-D-16-0253.1
Mainelli M, DeMaria M, Shay L K, et al. 2008. Application of oceanic heat content estimation to operational forecasting of recent Atlantic category 5 hurricanes. Weather and Forecasting, 23(1): 3–16, doi: 10.1175/2007WAF2006111.1
Mathur M B. 1998. Development of an eye-wall like structure in a tropical cyclone model simulation. Dynamics of Atmospheres and Oceans, 27(1–4): 527–547
Powell M D, Vickery P J, Reinhold T A. 2003. Reduced drag coefficient for high wind speeds in tropical cyclones. Nature, 422(6929): 279–283, doi: 10.1038/nature01481
Price J F. 1981. Upper ocean response to a hurricane. Journal of Physical Oceanography, 11(2): 153–175, doi: 10.1175/1520-0485(1981)011<0153:UORTAH>2.0.CO;2
Price J F, Sanford T B, Forristall G Z. 1994. Forced stage response to a moving hurricane. Journal of Physical Oceanography, 24(2): 233–260, doi: 10.1175/1520-0485(1994)024<0233:FSRTAM>2.0.CO;2
Riehl H. 1950. A model of hurricane formation. Journal of Applied Physics, 21(9): 917–925, doi: 10.1063/1.1699784
Riemer M, Montgomery M T, Nicholls M E. 2010. A new paradigm for intensity modification of tropical cyclones: thermodynamic impact of vertical wind shear on the inflow layer. Atmospheric Chemistry and Physics, 10(7): 3163–3188, doi: 10.5194/acp-10-3163-2010
Rotunno R, Emanuel K A. 1987. An air-sea interaction theory for tropical cyclones. Part II: Evolutionary study using a nonhydrostatic axisymmetric numerical model. Journal of the Atmospheric Sciences, 44(3): 542–561, doi: 10.1175/1520-0469(1987)044<0542:AAITFT>2.0.CO;2
Schade L R. 2000. Tropical cyclone intensity and sea surface temperature. Journal of the Atmospheric Sciences, 57(18): 3122–3130, doi: 10.1175/1520-0469(2000)057<3122:TCIASS>2.0.CO;2
Schade L R, Emanuel K A. 1999. The ocean's effect on the intensity of tropical cyclones: results from a simple coupled atmosphere-ocean model. Journal of the Atmospheric Sciences, 56(4): 642–651, doi: 10.1175/1520-0469(1999)056<0642:TOSEOT>2.0.CO;2
Shan Haixia, Dong Changming. 2019. Atmospheric responses to oceanic mesoscale eddies based on an idealized model. International Journal of Climatology, 39(3): 1665–1683, doi: 10.1002/joc.5908
Shapiro L J. 1982. Hurricane climatic fluctuations: Part II. Relation to large-scale circulation. Monthly Weather Review, 110(8): 1014–1023, doi: 10.1175/1520-0493(1982)110<1014:HCFPIR>2.0.CO;2
Shay L K. 2009. Upper ocean structure: responses to strong Atmospheric forcing events. In: Steele J H, ed. Encyclopedia of Ocean Sciences. 2nd ed. Amsterdam: Elsevier Press, 192–210
Shay L K. 2010. Air-sea interactions in tropical cyclones. In: Chan J C L, Kepert J D, eds. Global Perspectives on Tropical Cyclones: From Science to Mitigation. Singapore: World Scientific, 93–131
Shay L K, Brewster J K. 2010. Oceanic heat content variability in the eastern Pacific Ocean for hurricane intensity forecasting. Monthly Weather Review, 138(6): 2110–2131, doi: 10.1175/2010MWR3189.1
Shay L K, Goni G J, Black P G. 2000. Effects of a warm oceanic feature on hurricane Opal. Monthly Weather Review, 128(5): 1366–1383, doi: 10.1175/1520-0493(2000)128<1366:EOAWOF>2.0.CO;2
Skamarock W C, Klemp J B, Dudhia J, et al. 2008. A description of the advanced research WRF version 3. NCAR Technical Note, NCAR/TN-475+STR. Boulder: National Center for Atmospheric Research
Sun Jia, Wang Dingqi, Hu Xiaomin, et al. 2019. Ongoing poleward migration of tropical cyclone occurrence over the western North Pacific Ocean. Geophysical Research Letters, 46(15): 9110–9117, doi: 10.1029/2019GL084260
Sun Jia, Wang Guihua, Zuo Juncheng, et al. 2017a. Role of surface warming in the northward shift of tropical cyclone tracks over the South China Sea in November. Acta Oceanologica Sinica, 36(5): 67–72, doi: 10.1007/s13131-017-1061-8
Sun Yuan, Zhong Zhong, Ha Yao, et al. 2013. The dynamic and thermodynamic effects of relative and absolute sea surface temperature on tropical cyclone intensity. Acta Meteorologica Sinica, 27(1): 40–49, doi: 10.1007/s13351-013-0105-z
Sun Yuan, Zhong Zhong, Li T, et al. 2017b. Impact of ocean warming on tropical cyclone size and its destructiveness. Scientific Report, 7(1): 8154, doi: 10.1038/s41598-017-08533-6
Sun Yuan, Zhong Zhong, Yi Lan, et al. 2014. The opposite effects of inner and outer sea surface temperature on tropical cyclone intensity. Journal of Geophysical Research: Atmospheres, 119(5): 2193–2208, doi: 10.1002/2013JD021354
Sun Jia, Zuo Juncheng, Ling Zheng, et al. 2016. Role of ocean upper layer warm water in the rapid intensification of tropical cyclones: a case study of typhoon Rammasun (1409). Acta Oceanologica Sinica, 35(3): 63–68, doi: 10.1007/s13131-015-0761-1
Wadler J B, Zhang J A, Jaimes B, et al. 2018. Downdrafts and the evolution of boundary layer thermodynamics in Hurricane Earl (2010) before and during rapid intensification. Monthly Weather Review, 146(11): 3545–3565, doi: 10.1175/MWR-D-18-0090.1
Wang Yuqing. 2002. Vortex Rossby waves in a numerically simulated tropical cyclone: Part II. the role in tropical cyclone structure and intensity changes. Journal of the Atmospheric Sciences, 59(7): 1239–1262, doi: 10.1175/1520-0469(2002)059<1239:VRWIAN>2.0.CO;2
Wang Yuqing. 2009. How do outer spiral rainbands affect tropical cyclone structure and intensity?. Journal of the Atmospheric Sciences, 66(5): 1250–1273, doi: 10.1175/2008JAS2737.1
Willoughby H E, Marks F D Jr, Feinberg R J. 1984. Stationary and moving convective bands in hurricanes. Journal of the Atmospheric Sciences, 41(22): 3189–3211, doi: 10.1175/1520-0469(1984)041<3189:SAMCBI>2.0.CO;2
Wu C C, Lee C Y, Lin I I. 2007. The effect of the ocean eddy on tropical cyclone intensity. Journal of the Atmospheric Sciences, 64(10): 3562–3578, doi: 10.1175/JAS4051.1
Wu C C, Tu W T, Pun I F, et al. 2016. Tropical cyclone-ocean interaction in Typhoon Megi (2010)—A synergy study based on ITOP observations and atmosphere-ocean coupled model simulations. Journal of Geophysical Research: Atmospheres, 121(1): 153–167, doi: 10.1002/2015JD024198
Wu Liguang, Wang Bin, Braun S A. 2005. Impacts of air-sea interaction on tropical cyclone track and intensity. Monthly Weather Review, 133(11): 3299–3314, doi: 10.1175/MWR3030.1
Wu Liguang, Wang Ruifang, Feng Xiaofang. 2018. Dominant role of the ocean mixed layer depth in the increased proportion of intense typhoons during 1980–2015. Earth's Future, 6(11):

1518–1527, doi: 10.1029/2018EF000973

Yablonsky R M, Ginis I. 2012. Impact of a warm ocean eddy's circulation on hurricane-induced sea surface cooling with implications for hurricane intensity. Monthly Weather Review, 141(3): 997–1021

Yan Youfang, Li Li, Wang Chunzai. 2017. The effects of oceanic barrier layer on the upper ocean response to tropical cyclones. Journal of Geophysical Research: Oceans, 122(6): 4829–4844, doi: 10.1002/2017JC012694

Yang Guang, Wang Fan, Li Yuanlong, et al. 2013. Mesoscale eddies in the northwestern subtropical Pacific Ocean: statistical characteristics and three-dimensional structures. Journal of Geophysical Research: Oceans, 118(4): 1906–1925, doi: 10.1002/jgrc.20164

Yang Guang, Yu Weidong, Yuan Yeli, et al. 2015. Characteristics, vertical structures, and heat/salt transports of mesoscale eddies in the southeastern tropical Indian Ocean. Journal of Geophysical Research: Oceans, 120(10): 6733–6750, doi: 10.1002/2015JC011130

Zhang Zhengguang, Zhang Yu, Wang Wei, et al. 2013. Universal structure of mesoscale eddies in the ocean. Geophysical Research Letters, 40(14): 3677–3681, doi: 10.1002/grl.50736

Zhang Zhengguang, Wang Wei, Qiu Bo. 2014. Oceanic mass transport by mesoscale eddies. Science, 345(6194): 322–324, doi: 10.1126/science.1252418

Zhao Xiaohui, Chan J C L. 2017. Changes in tropical cyclone intensity with translation speed and mixed-layer depth: idealized WRF-ROMS coupled model simulations. Quarterly Journal of the Royal Meteorological Society, 143(702): 152–163, doi: 10.1002/qj.2905

Zweng M M, Reagan J R, Seidov D, et al. 2018. World Ocean Atlas 2018, Volume 2: Salinity. NOAA Atlas NESDIS 82. US: NOAA, 1–50